Journal of Air Pollution and Health (Spring 2019); 4(2): 87-98

Original Article

Available online at http://japh.tums.ac.ir

Numerical simulation of electrostatic field and flow field in an electrostatic precipitator

Yuying Xu, Baoqing Deng*, Haiyan Zhang, Xianpeng Chen

Department of Environmental Science and Engineering, University of Shanghai for Science and Technology, Shanghai 200093, P.R. China

ARTICLE INFORMATION

Article Chronology:
Received 15 April 2019
Revised 20 May 2019
Accepted 10 June 2019
Published 29 June 2019

Keywords:
CFD; Electrostatic precipitator

CORRESPONDING AUTHOR:

bqdeng@usst.edu.cn
Tel: 00862155271991
Fax: 008655271991

ABSTRACT:

Introduction: The computational fluid dynamics (CFD) simulation of three-dimensional wire-plate electrostatic precipitator is performed in the present study.

Materials and methods: The momentum equation, the electric potential equation and current continuity equation are solved by using ANSYS Fluent. The ion charge density at the corona is calculated iteratively using the Peek formula. The SIMPLE algorithm is used to treat the pressure-velocity coupling. The RNG *k-ε* model is used to describe turbulence.

Results: The airflow keeps stable away from the first corona electrode. The distribution of the electric potential is dependent on the wire-plate distance and the wire-wire distance. The potential and ion charge density increase with the increase of the wire-plate distance. With the increase of wire-wire distance, the maximum electric field strength decreases whereas the maximum ionic charge density increases. The ion charge density near the second corona electrode is relatively small. A small wire-wire distance will make the electric field concentrated around the wires.

Conclusion: According to this study, the wire-wire distance and the wire-plate distance have great effect on the distribution of ion charge density and electric field strength.

Introduction

The electrostatic precipitator (ESP) is a widely used device for particulate removal [1-5]. There exist complex physical processes in an ESP, including the turbulent flow, the ionization of air, the transport of particulate and the movement of electric charge. Ions are produced by corona discharge. Particles suspended in the air are charged by attachment of ions. Under the effect of electric force, charged particles in the air move to the dust collecting plate and deposit on it. The movement of particles in the ESP is affected by both the airflow and the electric force. Therefore, it is of great importance to predict the airflow and the electric field in the optimization of the ESP.

Several numerical methods have been developed to simulate the flow field, the space charge density and the electric field in the ESP, including the boundary element method [6], the finite differencing technique [7] and the finite volume method [8-10]. All these methods have achieved success in the simulation of the airflow in the ESP. However, the finite volume method has gained popu-

Please cite this article as: Xu Y, Deng B, Zhang H, Chen X. Numerical simulation of electrostatic field and flow field in an electrostatic precipitator. Journal of Air Pollution and Health. 2019; 4(2): 87-98.

larity in academic community due to its robustness and the applicability to complex geometry.

Many parameters can greatly affect the operation of the ESP. The most important parameter is the applied voltage, which determines the electrostatic field and thus corona discharge [11, 12]. The gas velocity determines the residence time of particles in the ESP and has a direct influence on the particle charging [11]. Inlet height, wire spacing and the precipitator structure may have effect on the gas velocity and thus particle charging in a wire-plate ESP [12]. Computational fluid dynamics (CFD) has been successfully used to simulate the flow field and the particle collection efficiency in the ESP [13]. On the other hand, ion mobility, ion diffusion coefficient and roughness of the electrode may greatly affect the voltage–intensity curve [14]. High resistivity particles were proved to affect the capture efficiency in a new type of ESP [15].

However, the characteristics of electrostatic field is different from the airflow field, which decays fast spatially. In this study, a CFD model is presented to simulate the turbulent airflow and the electrostatic field in the ESP. The effects of the wire-wire distance and wire-plate distance on the electrostatic field in the ESP is studied in detail.

Materials and methods

Mathematical model

Considering the velocity of air in the ESP, the air is assumed incompressible and the airflow is turbulent. Under the effect of electrostatic field, a corona discharge occurs. The produced ions attach to suspended particles. Thus, the electrostatic force is exerted on charged particles, which further has effect on the movement of air and charged particles. Under the Eulerian framework, the governing equations describing the airflow can be written as follows:

$$\frac{\partial u_j}{\partial x_j} = 0 \tag{1}$$

$$\frac{\partial}{\partial x_j}(\rho u_i u_j) = \frac{-\partial p}{\partial x_i} + \frac{\partial}{\partial x_j}\left[(\mu + \mu_t)\frac{\partial u_i}{\partial x_j}\right] + \rho_{ion} E_i \tag{2}$$

Where x_j is the coordinate component, u_j is the air velocity component (m/s), ρ is the air density (kg/m^3), μ_t is the turbulent viscosity (kg/m.s), ρ_{ion} is the ionic charge density (C/m^3), p is the pressure (pa), E_i is the electric field strength (V/m).

The third term in the right-hand side of Eq. (2) describes the effect of the electrostatic force. Its description requires the information of the electric field strength and the ion charge density. The electric field strength is defined as follows:

$$E_i = \frac{-\partial \varphi}{\partial x_i} \tag{3}$$

where φ is the electric potential (V). In the ESP, the electric potential can be described by the Poisson equation:

$$\frac{\partial^2 \varphi}{\partial x_j^2} = \frac{-\rho_{ion}}{\varepsilon_0} \tag{4}$$

where ε_0 is the permittivity of free space. On the other hand, the movement of particle charge is affected by the airflow and the electric field. The current continuity equation can be described as follows:

$$\frac{\partial}{\partial x_j}\left[\rho_{ion}\left(k_{ion} E_j + u_j\right)\right] = \frac{\partial}{\partial x_j}\left[D_e \frac{\partial \rho_{ion}}{\partial x_j}\right] \tag{5}$$

Where, D_e is the ion diffusion coefficient (m^2/s).

Numerical procedure

The airflow velocity, the turbulent intensity and the turbulent viscosity ratio are specified at the inlet. The pressure is specified at the outlet. At all walls, no-slip condition is given. At the corona, the electric potential is specified as the operating potential. At the dust collecting plate, the elec-

tric potential is set zero. At all other boundaries, the gradient of the electric potential is zero. The gradient of ion charge density is zero at the inlet, outlet and the dust collecting plate. At the corona electrode, the ion charge density is calculated iteratively until the Peek formula is satisfied, which writes

$$E_{peek} = 3.1 \times 10^6 m\delta\left(1 + \frac{0.03}{\sqrt{\delta r}}\right) \quad (6)$$

Where m is the polar line roughness coefficient, δ is the relative density with respect to the standard condition, r is the polar radius (m).

All governing equations are solved using the commercial software ANSYS Fluent. The SIMPLE algorithm is used to treat the pressure-velocity coupling. The RNG k-ε model is used to describe turbulence. All convection terms are discretized using the second-order upwind scheme. When the normalized residuals are less than 1×10^{-4}, the computation is assumed convergent.

Results and discussion

The present model is validated against the experimental data of Penny and Matick [16]. The operating voltage is 43.5 kV and the corona wire diameters are 0.03 cm. Fig. 1. shows the potential distribution at different locations. In general, the present simulation obtains good agreement with the experimental data. It shows that the present model has a good ability to simulate the electric field distribution in the ESP.

A wire-plate ESP with a length of 0.5 m, a width of 0.12 m and a height of 0.24 m is simulated, as shown in Fig. 2. Three corona electrodes with a diameter of 5 mm are positioned in the ESP. The operating voltage is 70 kV. The tetrahedral grid is used to discretize the computational domain, as shown in Fig. 3. Since the diameter of corona electrode is very small, the mesh is refined greatly in the vicinity of the corona electrode.

Fig. 4. shows the distribution of x velocity at different planes. As shown in Fig. 4(a), the air-

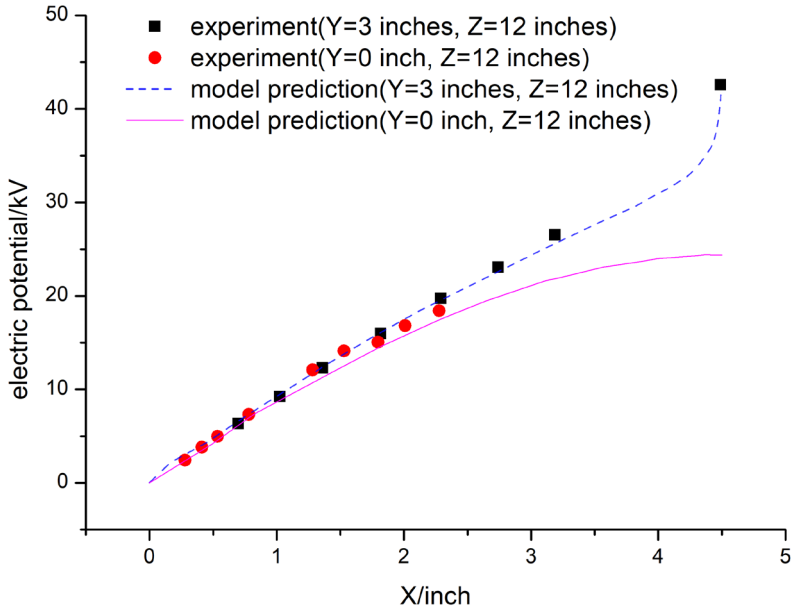

Fig. 1. The electric potential distribution in an ESP

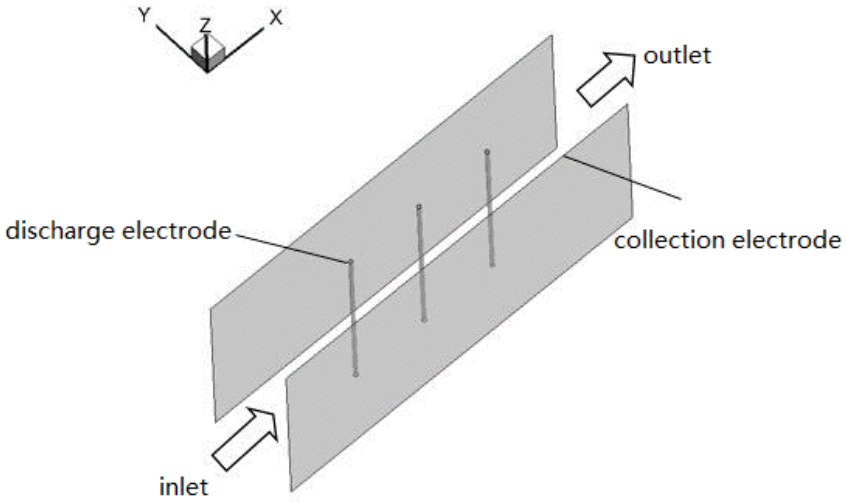

Fig. 2. Schematic of a 3D wire plate electrostatic precipitator

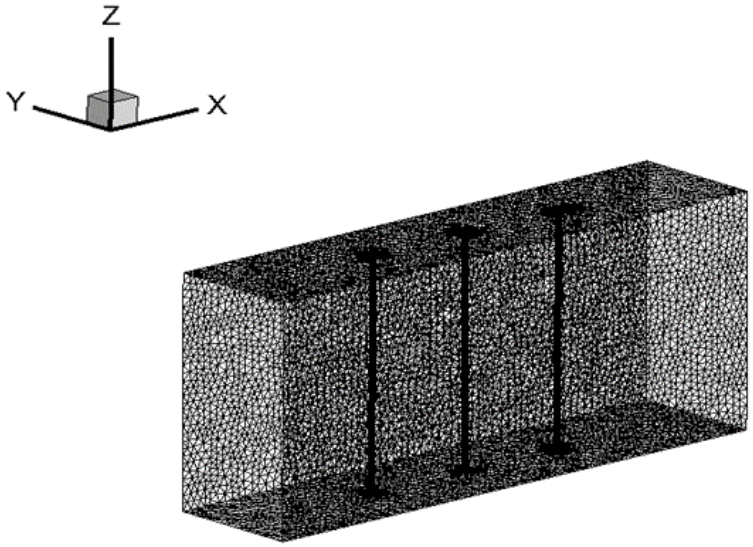

Fig. 3. Schematic of grid in an electrostatic precipitator

flow in the vicinity of the first corona electrode is chaotic and a 3D feature can be observed. The airflow near the first corona electrode depicts the typical feature of flow around cylinder, as shown in Fig. 4(b). After passing the first corona electrode, the airflow tends to be stable and the nearly same patterns are shown near the second and the third corona electrodes. Regions of low velocity are found behind the corona electrodes. The large velocity region is located between the corona electrode and the dust collecting electrode. The velocity in the central region of the channel is smaller due to the existence of corona electrodes.

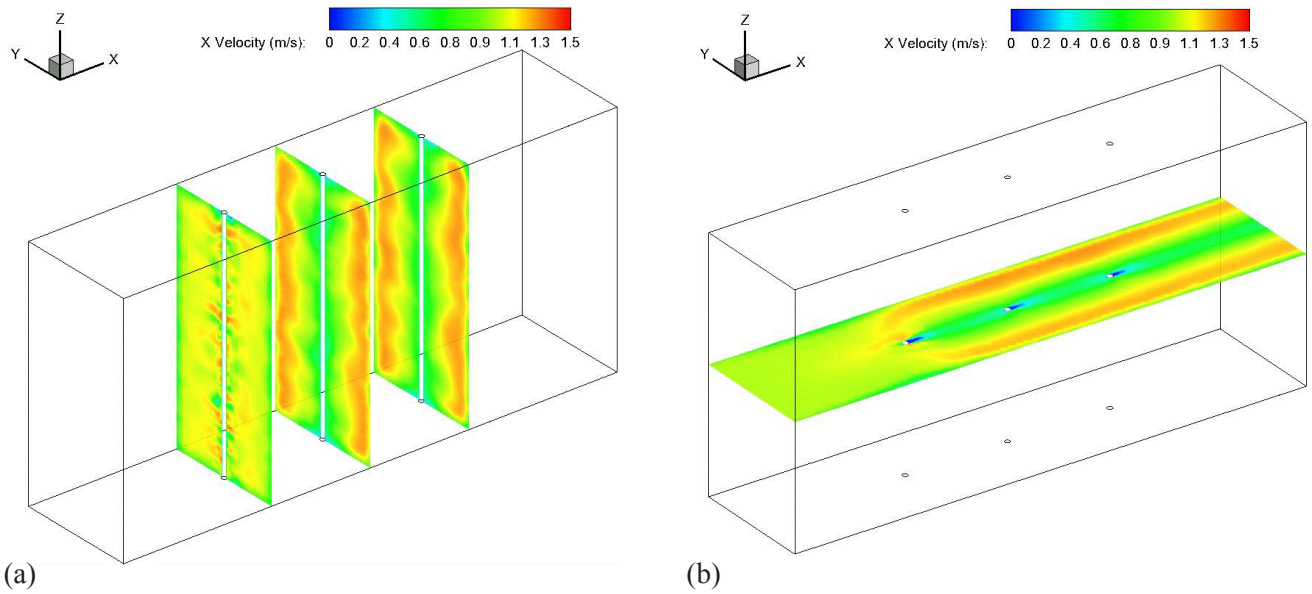

Fig. 4. Airflow patterns: (a) X = 0.15 m, 0.25 m, 0.35 m, (b) Z = 0.12 m

Fig. 5 illustrates the electric potential distribution at different planes. The same patterns of the electric potential distribution are observed near three corona electrodes, which means that the interaction among three corona electrodes is very weak due to a relatively large distance of two electrodes.

Fig. 6 shows the distribution of the electric field strength at different planes. The same tendency as the electric potential distribution is observed, which is in accordance with the definition of electric field strength, i.e., Eq. (3).

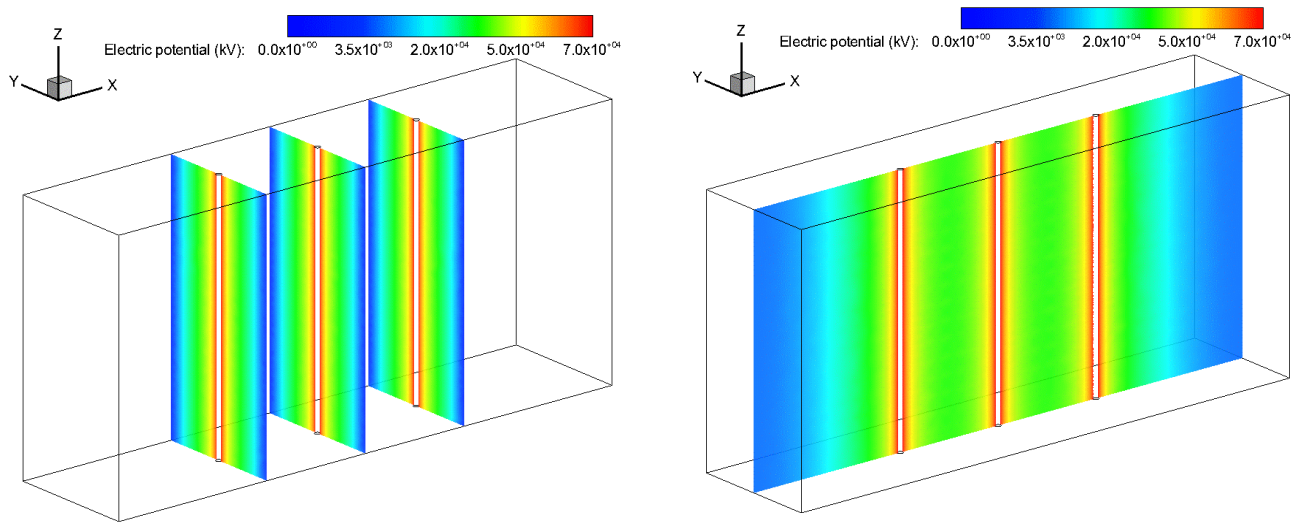

Fig. 5. The electric potential distribution: (a) X = 0.15 m, 0.25 m, 0.35 m, (b) Y = 0.06 m

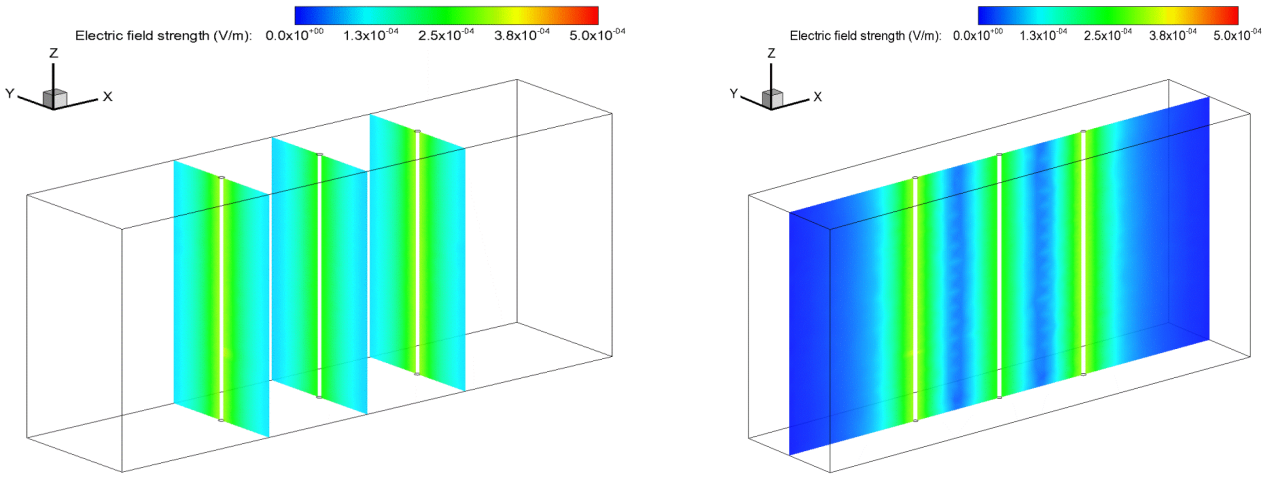

Fig. 6. The electric field intensity distribution: (a) X = 0.15 m, 0.25 m, 0.35 m, (b) Y = 0.06 m

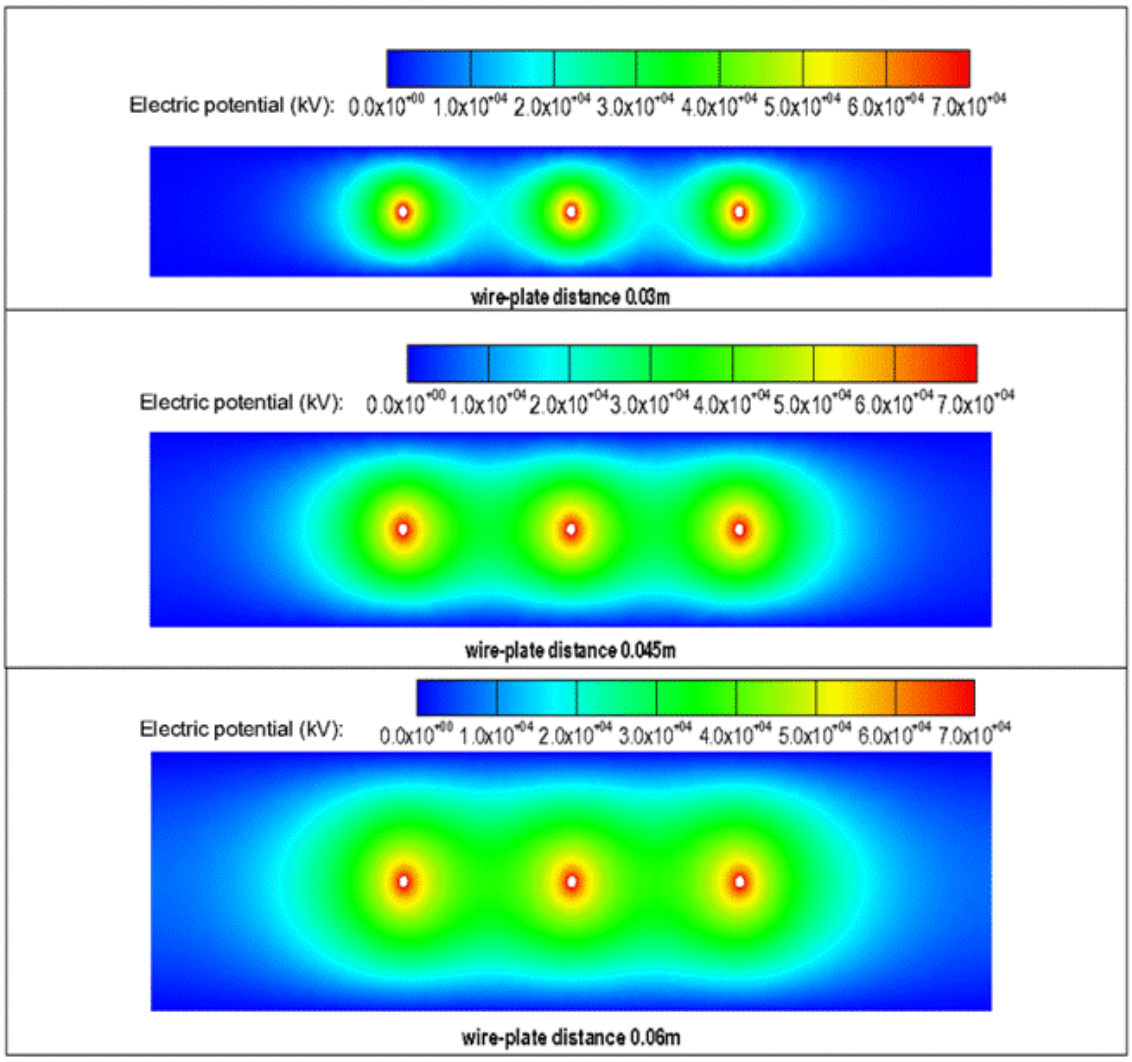

Fig. 7. The electric potential distributions for different wire-plate distances at Z=0.12 m

The electric potential distribution at the plane Z=0.12 m for different wire-plate distances is shown in Fig. 7. The region of high potential increases with the increase of the wire-plate distance. For a large wire-plate distance, the region of large potential for each wire overlaps and connects with each other, which may decrease the electric field strength between corona electrodes. Fig. 8. depicts the electric field strength at the plane Z=0.12 m for different wire-plate distances. There exists a large region of small electric field strength between corona electrodes for a large wire-plate distance, which is in accordance with the prediction of Fig. 7. For a large wire-plate distance, the distribution of electric field strength tends to be circular and the region of large electric field strength tends to be small. For a small wire-plate distance, there is a continuous region of large electric field strength, which may help to the movement of particles to the dust collecting electrode.

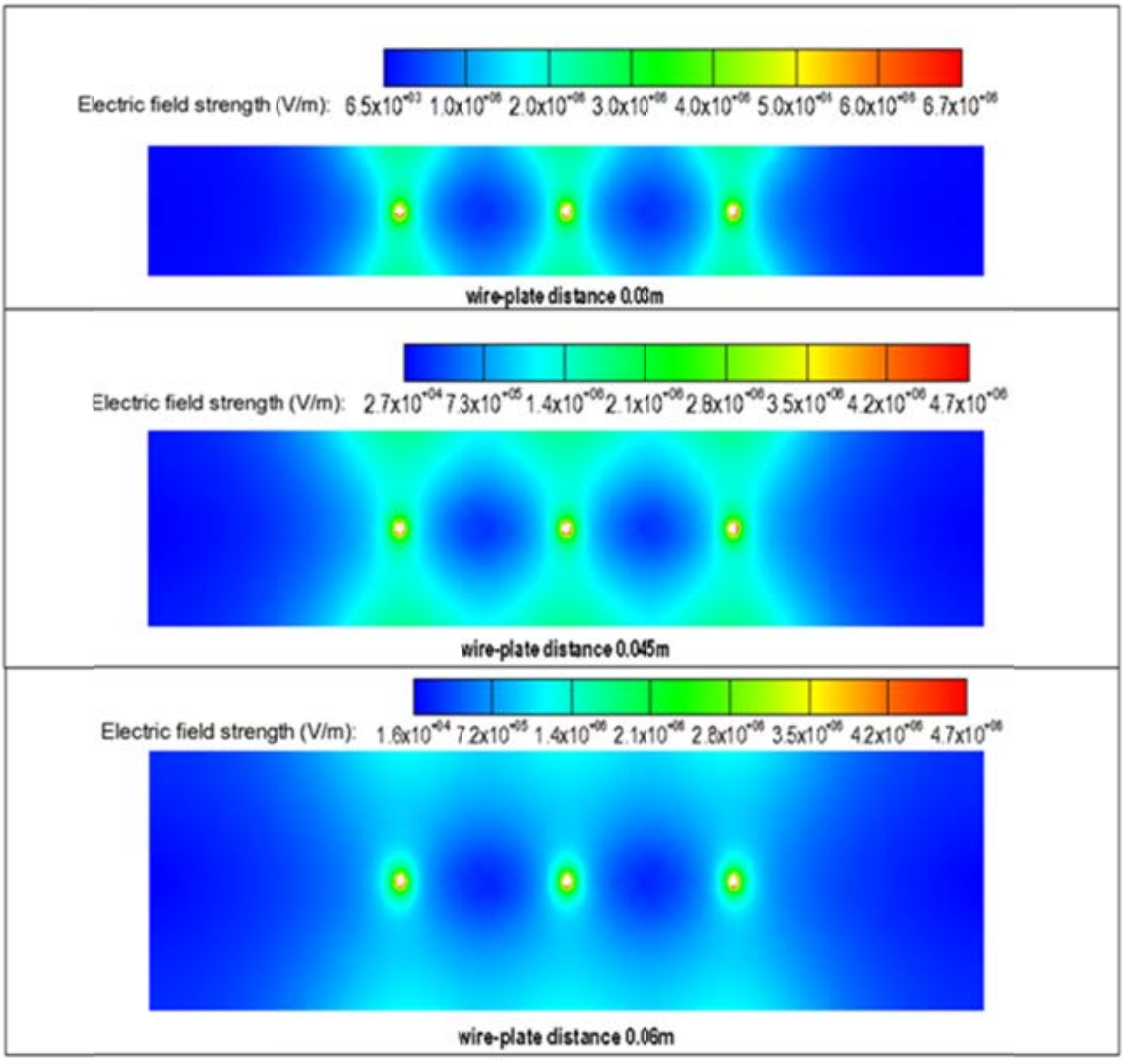

Fig. 8. The electric field intensity distributions for different wire-plate distances at Z=0.12 m

The distribution of ion charge density is illustrated in Fig. 9. In the vicinity of the wire, a circular pattern of the ion charge density is depicted for all three distances. With the increase of the wire-plate distance, the region of large ion charge density becomes larger in the streamwise direction, and the ion charge density near the second corona electrode becomes smaller.

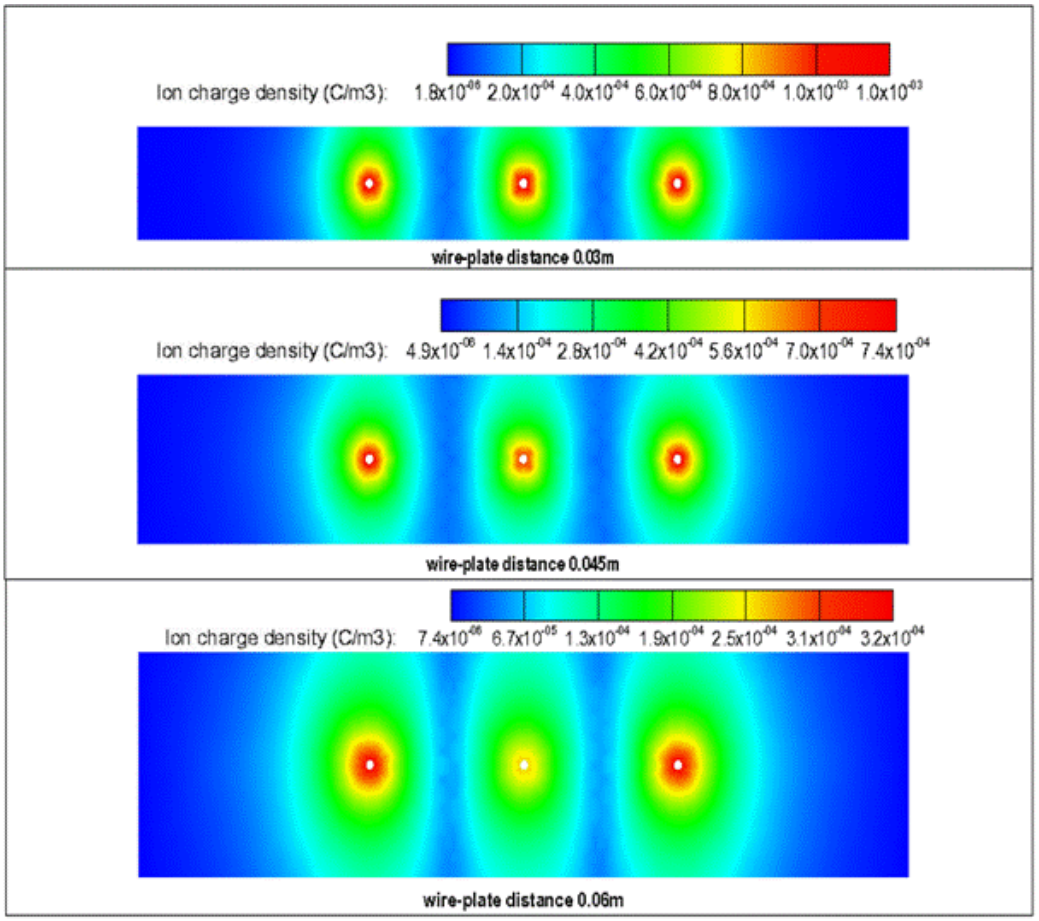

Fig. 9. The ion charge density distributions for different wire-plate distances at Z = 0.12 m

Fig. 10 shows the potential distribution at the plane Z=0.12 m for different wire-wire distances. As the wire-wire distance increases, the potential distribution tends to be oval near the corona electrode and the region of high potential becomes large. When the wire-wire distance is large enough, the potential at the inlet and outlet will increase. For a small wire-wire distance, the region of high potential will be concentrated.

Fig. 11 displays the electric field strength distribution at the plane Z=0.12 m for different wire-wire distances. The nearly same patterns are observed near each wire. The wire-wire distance has little influence on the electric field strength distribution between wires. For a small wire-wire distance, the electric field is concentrated around the wires, outside which the electric force on charged particles may be very small.

Fig. 12 illustrates the distribution of ion charge density at Z=0.12 m for different wire-wire dis-

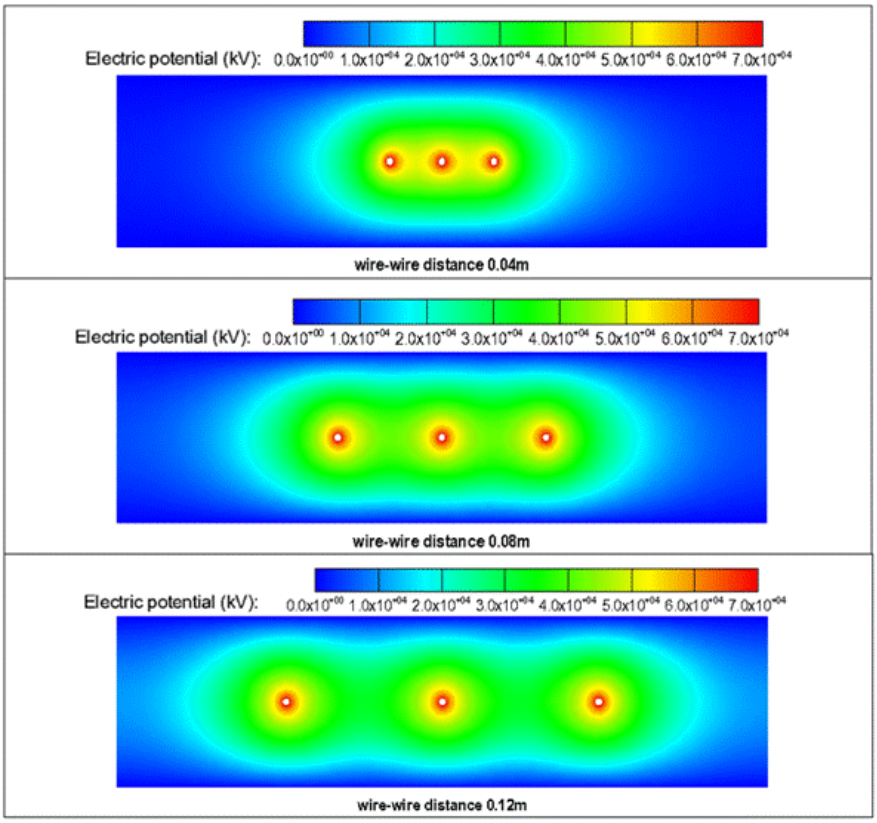

Fig. 10. The electric potential distributions for different wire-wire distances at Z = 0.12 m

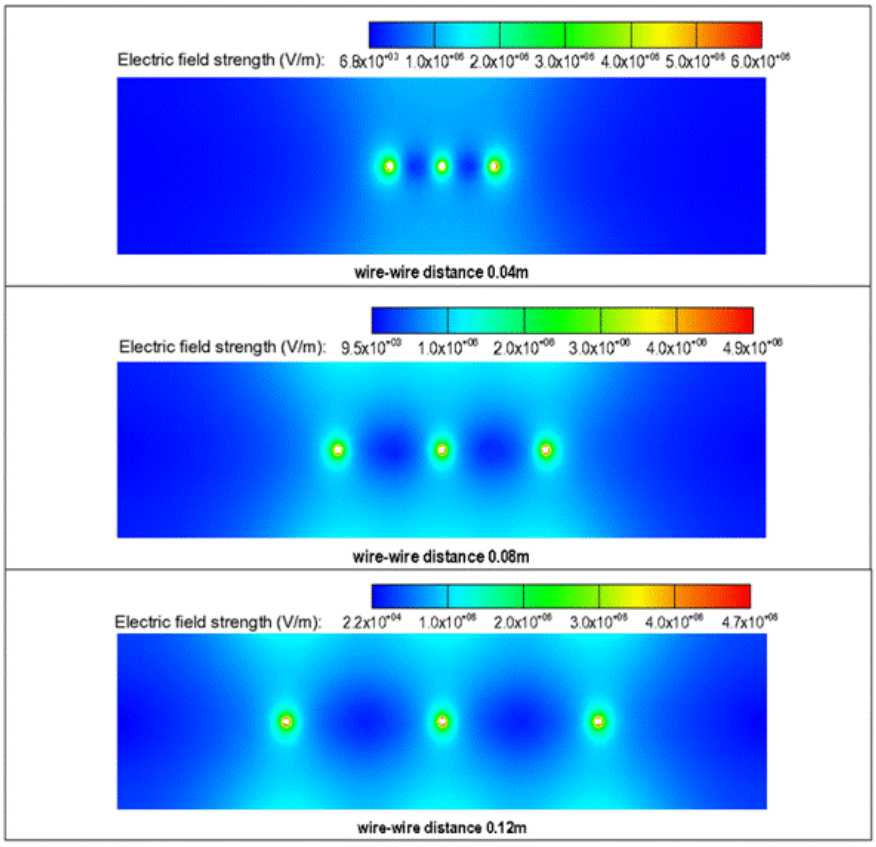

Fig. 11. The electric field intensity distributions for different wire-wire distances at Z = 0.12 m

tances. With the decrease of wire-wire distance, the maximum ion charge density becomes small, and the maximum ion charge density for the middle wire is much smaller than those for the other two wires. When the wire-wire distance is 0.04 m, the region of large ion charge density near the first and third wires become larger whereas the ion charge density becomes very small near the middle wire. When the wire-wire distance increases, the wires tend to be operated independently.

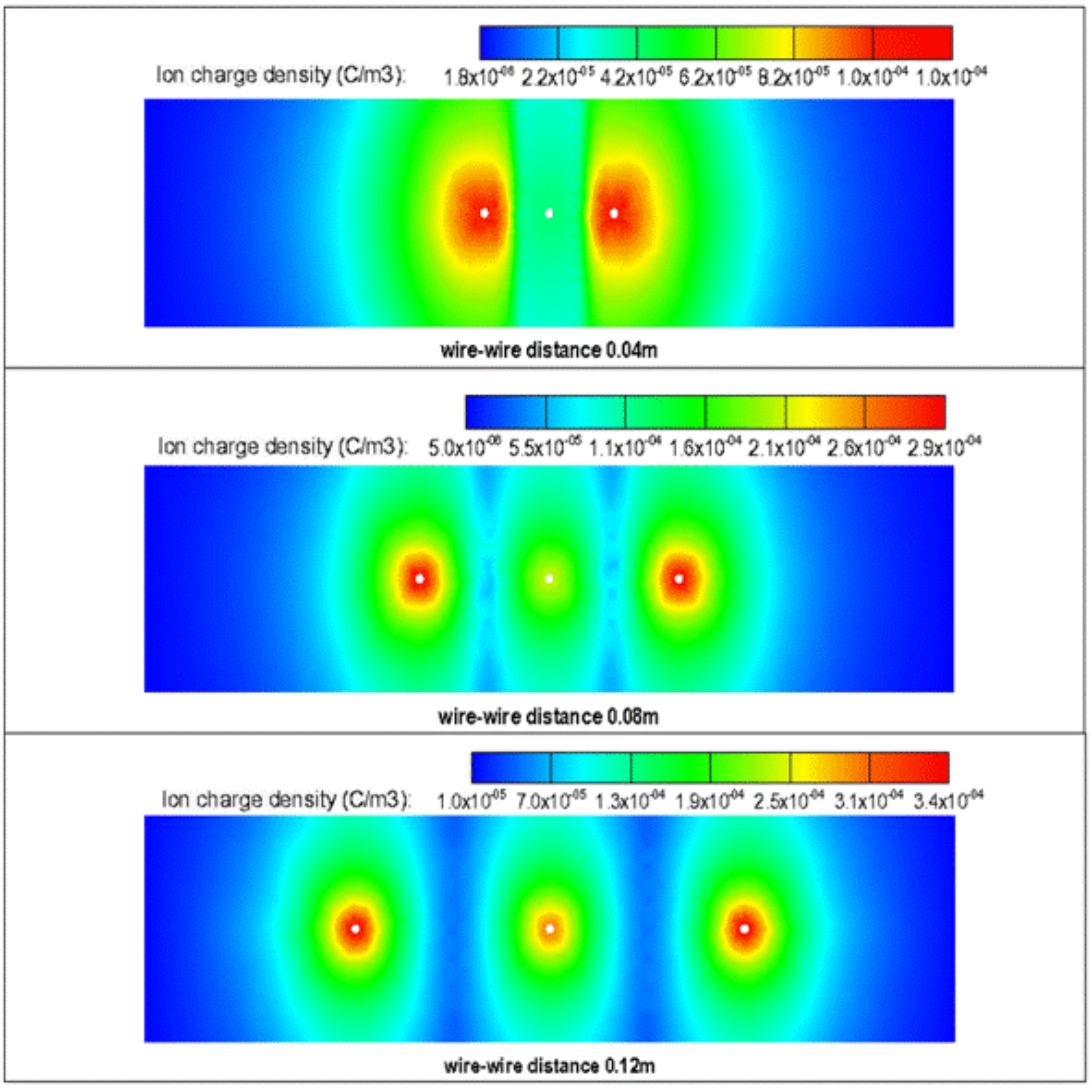

Fig. 12. The ion charge density distributions for different wire-wire distances at Z = 0.12 m

Conclusion

A CFD model is developed to investigate the flow field and the characteristics of electrostatic field in the ESP. Good agreement between the present computation and the experimental data is obtained. Except for the flow near the first corona electrode, a stable pattern of airflow exists in the ESP channel. The distribution of the electric potential near three corona electrodes are similar.

With the increase of the wire-plate distance, the region of high potential and the region of large ion charge density are enlarged in the streamwise direction, and thus the electric field strength between the corona electrodes tends to decrease. The ion charge density near the second corona electrode also decreases.

As the wire-wire distance increases, the maximum electric field strength decreases whereas the maximum ionic charge density increases. The potential distribution tends to be oval near the corona electrode. For a small wire-wire distance, the electric field is concentrated around the wires.

Financial supports

The authors would like to thank the financial support by Natural Science Foundation of Shanghai (No. 17ZR1419200).

Competing interests

The authors declare that there are no competing interests.

Acknowledgements

We would like to thank Prof. Fei Chang in Department of Environmental Science and Engineering for his insight on this project.

Ethical considerations

"Ethical issues (Including plagiarism, Informed Consent, misconduct, data fabrication and/or falsification, double publication and/or submission, redundancy, etc.) have been completely observed by the authors."

References

1. Chen T-M, Tsai C-J, Yan S-Y, Li S-N. An efficient wet electrostatic precipitator for removing nanoparticles, submicron and micron-sized particles. Separation and Purification Technology. 2014; 136:27–35.
2. Zhu J, Zhao Q, Yao Y, Luo S, Guo X, Zhang X, et al. Effects of high-voltage power sources on fine particle collection efficiency with an industrial electrostatic precipitator. Journal of Electrostatics. 2012; 70(3):285–91.
3. Kim J-H, Lee H-S, Kim H-H, Ogata A. Electrospray with electrostatic precipitator enhances fine particles collection efficiency. Journal of Electrostatics. 2010; 68(4):305–10.
4. Bin H, Lin Z, Yang Y, Fei L, Cai L, Linjun Y. $PM_{2.5}$ and SO_3 collaborative removal in electrostatic precipitator. Powder Technology. 2017; 318:484–90.
5. Qi L, Yuan Y. Influence of SO_3 in flue gas on electrostatic precipitability of high-alumina coal fly ash from a power plant in China. Powder Technology. 2013; 245:163–7.
6. Adamiak K. Simulation of corona in wire-duct electrostatic precipitator by means of the boundary element method. IEEE Transactions. on Ind. 1994; 30(2):381–6.
7. Anagnostopoulos J, Bergeles G. Corona discharge simulation in wire-duct electrostatic precipitator. Journal of Electrostatics. 2002; 54(2):129–47.
8. Choi BS, Fletcher CAJ. Computation of particle transport in an electrostatic precipitator. Journal of Electrostatics 1997; 40(Supplement C):413–8.
9. Neimarlija N, Demirdžić I, Muzaferija S. Finite volume method for calculation of electrostatic fields in electrostatic precipitators. Journal of Electrostatics. 2009; 67(1):37–47.
10. Zhang X, Wang L, Zhu K. Particle tracking and particle-wall collision in a wire-plate electrostatic precipitator. Journal of Electrostatics. 2005; 63(11):1057–71.
11. Lu Q, Yang Z, Zheng C, Li X, Zhao C, Xu X et al. Numerical simulation on the fine particle charging and transport behaviors in a wire-plate electrostatic precipitator. Advanced Powder Technology. 2016; 27(5):1905–11.
12. Dong M, Zhou F, Zhang Y, Shang Y, Li S. Numerical study on fine-particle charging and transport behaviour in electrostatic precipitators. Powder Technology. 2018; 330:210–8.
13. Guo B-Y, Yu A-B, Guo J. Numerical modeling of electrostatic precipitation: Effect of Gas temperature. Journal of Aerosol Science. 2014; 77:102–15.
14. Porteiro J, Martín R, Granada E, Patiño D. Three-dimensional model of electrostatic precipitators for the estimation of their particle collection efficiency. Fuel

Processing Technology. 2016; 143:86–99.
15. Kherbouche F, Benmimoun Y, Tilmatine A, Zouaghi A, Zouzou N. Study of a new electrostatic precipitator with asymmetrical wire-to-cylinder configuration for cement particles collection. Journal of Electrostatics. 2016; 83:7–15.
16. Penney GW, Matick RE. Potentials in D-C corona fields. Trans. AIEE, Part I: Comm. Electron. 1960; 79(2):91–9.